University Library



A gateway to Melbourne's research publications

Minerva Access is the Institutional Repository of The University of Melbourne

Author/s:
Li, Z;Mao, X;Feng, D;Li, M;Xu, X;Luo, Y;Zhuang, L;Lin, R;Zhu, T;Liang, F;Huang, Z;Liu, D;Yan, Z;Du, A;Shao, Z;Zhu, Z

Title:
Prediction of perovskite oxygen vacancies for oxygen electrocatalysis at different temperatures

Date:
2024-12-01

Citation:
Li, Z., Mao, X., Feng, D., Li, M., Xu, X., Luo, Y., Zhuang, L., Lin, R., Zhu, T., Liang, F., Huang, Z., Liu, D., Yan, Z., Du, A., Shao, Z. & Zhu, Z. (2024). Prediction of perovskite oxygen vacancies for oxygen electrocatalysis at different temperatures. Nature Communications, 15 (1), pp.9318-. https://doi.org/10.1038/s41467-024-53578-7.

Persistent Link:
https://hdl.handle.net/11343/359115

License:
CC BY-NC-ND

nature communications

Article

https://doi.org/10.1038/s41467-024-53578-7

Prediction of perovskite oxygen vacancies for oxygen electrocatalysis at different temperatures

Received: 10 April 2024

Accepted: 16 October 2024

Published online: 29 October 2024

Check for updates

Zhiheng Li[1,2,3,10], Xin Mao[4,10], Desheng Feng[1,10], Mengran Li[5] ✉, Xiaoyong Xu[1,6] ✉, Yadan Luo[7] ✉, Linzhou Zhuang[8], Rijia Lin[1], Tianjiu Zhu[1], Fengli Liang[1], Zi Huang[7], Dong Liu[3], Zifeng Yan[3], Aijun Du[4], Zongping Shao[9] ✉ & Zhonghua Zhu[1] ✉

Efficient catalysts are imperative to accelerate the slow oxygen reaction kinetics for the development of emerging electrochemical energy systems ranging from room-temperature alkaline water electrolysis to high-temperature ceramic fuel cells. In this work, we reveal the role of cationic inductive interactions in predetermining the oxygen vacancy concentrations of 235 cobalt-based and 200 iron-based perovskite catalysts at different temperatures, and this trend can be well predicted from machine learning techniques based on the cationic lattice environment, requiring no heavy computational and experimental inputs. Our results further show that the catalytic activity of the perovskites is strongly correlated with their oxygen vacancy concentration and operating temperatures. We then provide a machine learning-guided route for developing oxygen electrocatalysts suitable for operation at different temperatures with time efficiency and good prediction accuracy.

Oxygen electrocatalysis predetermines the efficiency of the emerging electrochemical energy storage and conversion processes involving either oxygen reduction reaction (ORR) or oxygen evolution reaction (OER) over electrodes, such as metal-air batteries[1], electrolyzers[2,3], and fuel cells[4], These energy technologies are designed to be operated at different temperatures ranging from room temperature for polymer exchange membrane fuel cells[5], alkaline water electrolysis[6], and metal-air batteries[1] up to 1000 °C for solid oxide fuel cells and electrolysis cells[7–9]. Therefore, matching the oxygen electrocatalyst design to their targeted operating temperatures is imperative for the development of efficient and robust electrochemical energy systems at a scale.

Perovskite oxides with a general formula of ABO_3 are a versatile category of functional materials that have been extensively exploited as electrocatalysts for oxygen activation at a wide range of temperatures towards application in various energy conversion and storage devices[10–13]. The promise of these materials is closely related to the high flexibility of compositional cations at A- and B-sites, leading to the discovery of a wide range of material candidates for oxygen electro-

[1]School of Chemical Engineering, The University of Queensland, Brisbane, Australia. [2]Center of Artificial Photosynthesis for Solar Fuels and Department of Chemistry, School of Science and Research Center for Industries of the Future, Westlake University, Hangzhou, China. [3]School of Chemical Engineering, China University of Petroleum, Qingdao, China. [4]School of Chemistry and Physics and Centre for Materials Science, Queensland University of Technology, Brisbane, Australia. [5]Department of Chemical Engineering, The University of Melbourne, Melbourne, Australia. [6]School of Chemical Engineering, The University of Adelaide, Adelaide, Australia. [7]School of Information Technology and Electrical Engineering, The University of Queensland, Brisbane, Australia. [8]School of Chemical Engineering, East China University of Science and Technology, Shanghai, China. [9]WASM: Minerals, Energy and Chemical Engineering, Curtin University, Perth, Australia. [10]These authors contributed equally: Zhiheng Li, Xin Mao, Desheng Feng. ✉e-mail: aaron.li1@unimelb.edu.au; xiaoyong.xu@adelaide.edu.au; y.luo@uq.edu.au; zongping.shao@curtin.edu.au; z.zhu@uq.edu.au

catalysts operating at different temperatures in the past decades[14–17]. However, such flexible composition poses a challenge to the experiment-based catalyst material screening process, which is usually time-consuming and labor-intensive.

More recently, new strategies, such as machine learning and theory-based descriptors, have attracted considerable research attention for the rational development of materials, which has the potential to increase screening efficiency greatly[18–22]. Due to different reaction mechanisms, the performance of an electrocatalyst could vary vastly at different temperatures. For example, $Ba_{0.5}Sr_{0.5}Co_{0.8}Fe_{0.2}O_{3-\delta}$ (BSCF) was demonstrated to be a benchmark electrocatalyst for ORR at intermediate temperatures (600–800 °C), while it becomes an OER-active but ORR-poor electrocatalyst at room temperature in alkaline solution[8,23,24]. Nonetheless, the recently reported descriptors are only limited to a certain temperature or a narrow temperature range, which remains ineffective in predicting material behaviors at different temperatures. As such, the development of a universal method is in great demand but remains limited to enable the rational design of catalyst materials suiting a wide temperature range.

Previous findings have shown that the lattice oxygen (or oxygen vacancy) in the perovskite bulk can participate in the oxygen electrocatalysis process even at room temperature[25], and such bulk properties play a significant role in oxygen electrocatalysis at elevated temperatures. The formation of oxygen vacancies is closely related to the states of the redox-active transition metals at the B-site. Prior efforts, including ours[8,12,20,26], have shown that the cations at A-sites and dopants at B-sites can influence the states of these redox-active transition metals[27], and thus determine the oxygen vacancy concentration. Such cation-cation interactions can be interpreted as inductive effects as proposed by Noll[28] in 1963. By taking the inductive effects into account, we posit that the lattice cationic environment should have an inverse impact on the states of the catalytically active cations (e.g., cobalt and iron), and consequently, determine the formation of oxygen vacancies and oxygen activation kinetics. Hence, opportunities should exist to predict the oxygen vacancy concentration at different temperatures by determining the states of their lattice cationic environment constituted by the B-site dopants and A-site cations.

In this work, we apply machine learning techniques to explore the relationship between the lattice cationic environment and the concentration of oxygen vacancies at a wide range of temperatures. Our results show that the temperature-dependent concentration of the oxygen vacancies of cobalt-based or iron-based perovskites can be easily predicted from the well-established element properties, with no requirement for heavy computational cost. The oxygen electrocatalytic activity of perovskite metal oxides presents a "volcano" dependence on the concentration of oxygen vacancies, where the optimal oxygen vacancy concentration for electrocatalysis varies with the operating temperatures. We then used this machine learning-based strategy to develop new perovskite materials for low-temperature solid oxide fuel cells (SOFCs). Lowering the operating temperatures (e.g., ≤ 500 °C) is meaningful to address the challenge faced by existing high-temperature SOFC technologies, such as thermal cycling stability, sealing, and sluggish start-up/shut-down procedures[29]. Combining machine learning prediction with oxygen vacancy-activity relations, this work provides an alternative route to efficiently predict perovskite materials for electrocatalysis operated under a wide temperature range.

Results

Predicting oxygen vacancy concentration in perovskite oxides at a wide temperature range

Figure 1a presents the overall workflow applied in predicting the concentration of oxygen vacancies within the perovskite metal oxides via machine learning. The oxygen non-stoichiometry (denoted as δ) quantifies the concentration of the oxygen vacancies and thus serves as the targeted property for the model. We have included seven inputted features to feed the machine-learning models. Six of the features, reflecting the intrinsic properties of cations at A-sites and dopants at B-sites, are used to map the properties of the lattice cationic environment of perovskites, including tolerance factor (τ), electronegativity (χ), polarization power (P), charge (Z), and cation sizes for A-site (r_A) and B-site cations (r_B)[14,30–32]. All these features can be obtained from the database established by Shannon[33], Pauling[34], and Matar[35], and their values are weighted by the stoichiometries of the corresponding cations (see Supplementary Note 1). We also chose the operating temperature as another input to allow the prediction of the equilibrium concentration of oxygen vacancies within the oxide lattice at different temperatures.

To train and validate the models, we collected reported data from 235 cobalt-based (> 3000 data points) and 200 iron-based perovskite oxides (> 2500 data points) datasets. The collected data can represent the state-of-the-art perovskite oxides, and all these samples are in perovskite structures with disordered oxygen vacancies. The machine learning models randomly selected 80 % of the collected data for training and the rest 20 % samples for the test. 36 different algorithms were first implemented to fit the training data and were ranked based on the averaged coefficient of determination (R^2 score) from five random tests. Detailed ranking of these models is listed in Supplementary Fig. S1. We then selected one of the best-performing algorithms (*i.e.*, the one exhibiting the highest R^2 score), the LGBM regressor, as the model to predict the oxygen vacancies in our study.

Figure 1b and Fig. 1c present an excellent correlation between the predicted and reported oxygen vacancy concentrations for both cobalt- and iron-based perovskite oxides, which is evidenced by the close-to-unity slope of the trendline, high R^2 value (0.92 for cobalt-based and 0.92 for iron-based materials) (Supplementary Fig. S1a) as well as a low value of Root Mean Square Error (RMSE = 0.044), which refers to the average magnitude of the difference between predicted and actual values (Supplementary Fig. S1b). Interestingly, other regression algorithms, such as the Hist-Gradient-Boosting regressor, Random Forest Regressor and XGB-regressor (Supplementary Fig. S1a), can also achieve a good prediction ($R^2 > 0.90$, RMSE < 0.05). These good predictions confirm that the lattice cationic environment plays a vital role in predetermining the concentration of oxygen vacancies at a wide temperature range, even though they are not directly involved in the formation of oxygen vacancies. Note that Co- and Fe-based oxides are mainly explored in this work because of their large dataset size, and other active metal-containing perovskites should also show similar prediction trend if sufficient data are available. The ML model in this work is thus limited in predicting the oxygen vacancies for other transition metals (e.g., Cr, Mn) containing perovskites.

To further elucidate the role of the lattice cationic environment in the oxygen vacancy formation, we evaluated the correlation of each inputted feature with the oxygen vacancies by using partial dependence analysis from the LGBM regressor (Supplementary Fig. S2) and Shapley Additive Explanations (SHAP) feature importance analysis (Supplementary Fig. S3). The results reveal that the creation of the oxygen vacancies is more dependent on the electronegativity, polarization power, charge, and temperature than the tolerance factor, A-site cation and B-site dopant sizes for cobalt-based perovskites. More importantly, the identified correlation from the analyzes matches well with previously reported strategies effective for the creation of oxygen vacancies. For example, the oxygen vacancies can be created if the temperature increases[36] or if the lattice cationic environment shows a low charge[37,38], high polarization power[14], low electronegativity[39], and large A-site or B-site cations[40]. In the following section, we applied density functional theory (DFT) to explain how the lattice cationic environment predetermines the formation of oxygen vacancies.

https://doi.org/10.1038/s41467-024-53578-7

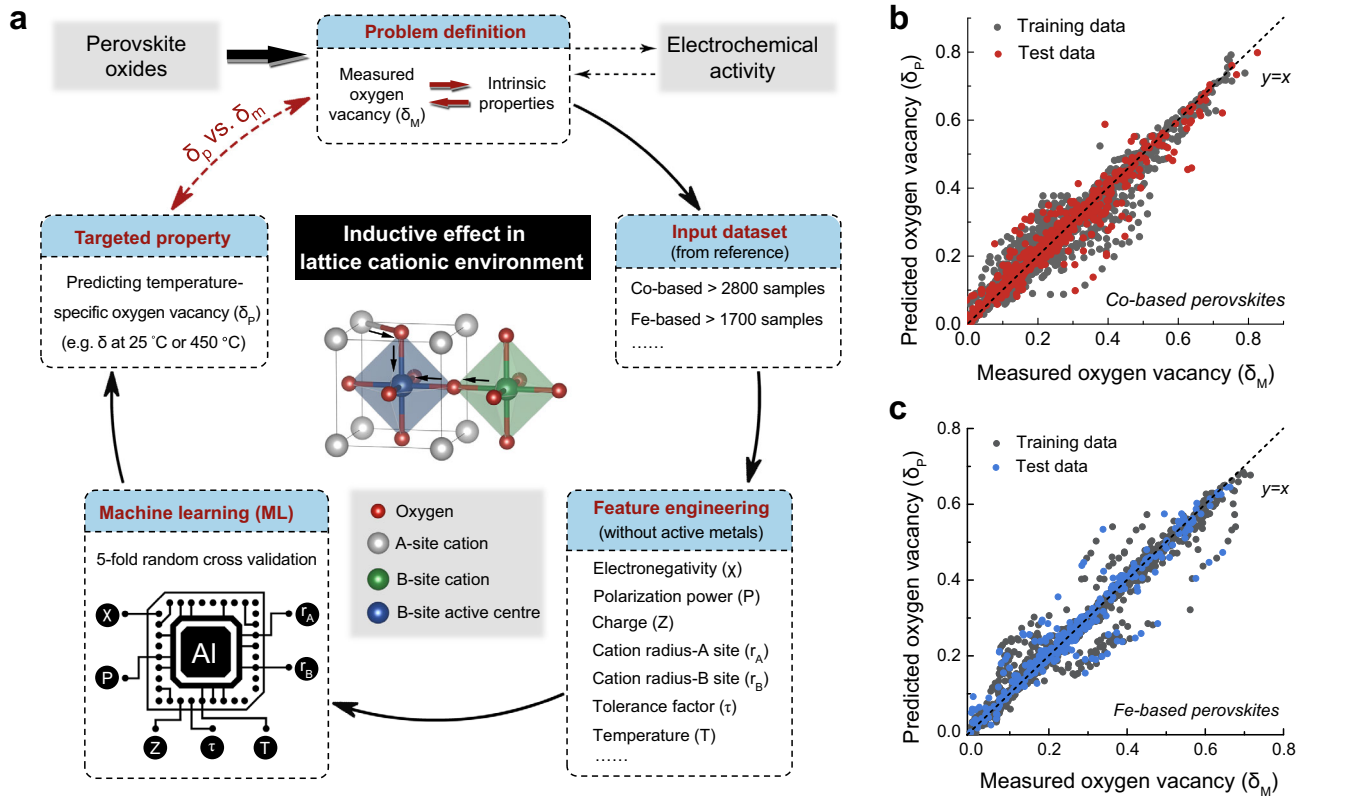


Fig. 1 | Machine learning (ML) assisted prediction of the oxygen vacancy concentration of perovskite oxides. a Workflow of the prediction of the oxygen vacancies of the $ABO_{3-\delta}$ perovskites at different temperatures. **b**, **c** Comparison of the measured (δ_M) and predicted oxygen vacancy (δ_P) for (**b**) cobalt-based and (**c**) iron-based perovskite oxides.

Elucidating the role of the lattice cationic environment on oxygen vacancy formation

In most of the perovskite oxides, the oxygen vacancies are usually created close to the redox-active elements such as cobalt[41], iron[42], chromium[43], and copper[44]. The lattice cationic environment should determine the concentration of oxygen vacancies by affecting the states of the active metal centers. To further probe the impacts of the lattice cationic environment on the state of the active metal centers, we performed DFT calculations over three cobalt-based perovskite models with different lattice cationic environments: $LaCoO_3$, $SrNb_{0.2}Co_{0.8}O_3$, and $SrCoO_3$. The simulation results shown in Supplementary Fig. S4 reveal a delocalization of the electrons at the cobalt centers for all three models. We also confirmed this delocalized fashion of electron distribution from the results obtained through Goodenough's approach[45] (Supplementary Fig. S5). Both results imply that the cobalt state in the lattice is a collective property, which can be profoundly influenced by the surrounding lattice cationic environment.

The interactions between the active metal centers and the lattice environment originate from the orbital overlaps (e.g., p-d and d-d orbitals) between cation and oxygen ions. Taking the three studied models as an example, if the lattice cationic environment is weak in attracting electrons (*e.g.*, Sr^{2+} *c.f.* La^{3+} as A-site host or Nb^{5+} at B-site), the cobalt tends to share electrons with the oxygen ions, leading to a high cobalt-oxygen covalency and thereby an easy charge transfer from oxygen to the cobalt to create oxygen vacancy (see Eq. (1)). This trend is consistent with our simulation results as shown in Supplementary Fig. S4d: oxygen vacancy is more easily created, as evidenced from the upshift of oxygen p-band center to the Fermi level, in the order of $LaCoO_{3-\delta} < SrNb_{0.2}Co_{0.8}O_{3-\delta} < SrCoO_{3-\delta}$. The strong interaction between the active metal centers and lattice cationic environment could be the main reason to enable us to predict the concentration of oxygen vacancies of the perovskite oxides at different temperatures.

$$2Co_{Co}^{\times} + O_O^{\times} \rightarrow 2Co_{Co}' + V_O'' + \frac{1}{2}O_2 \quad (1)$$

where $Co_{Co}^{\times}$ is a cobalt cation at the lattice site with a neutral charge, Co_{Co}' is a cobalt ion at a lattice site with one negative charge, $O_O^{\times}$ is oxygen ion at lattice with a neutral charge, V_O'' is oxygen vacancy with two positive charges, and O_2 is molecular oxygen.

The correlation between oxygen vacancy and activity for perovskite electrocatalysis

It is well known at elevated temperatures, the oxygen vacancies usually directly participate in the catalysis, so the concentration of oxygen vacancies serves as an important factor in predetermining the catalyst activity. In addition to the elevated temperature oxygen electrocatalysis, oxygen vacancies may also play an important role in room temperature oxygen electrocatalysis. Actually, many researches have demonstrated the lattice oxygen participation in room-temperature electrocatalytic water oxidation[46–48]. Based on the literature results, as shown in Supplementary Fig. S6, we found that the intrinsic activity of the state-of-the-art perovskite oxides for water oxidation showed a volcano trend as a function of the oxygen vacancies. This observed trend strongly supports the direct participation of the lattice oxygen in the OER, even at room temperature.

With the increase in operating temperature, an enhanced role of oxygen vacancies in the electrocatalytic process is expected. Here, we chose cobalt-based perovskites as the model catalyst to illustrate the

https://doi.org/10.1038/s41467-024-53578-7

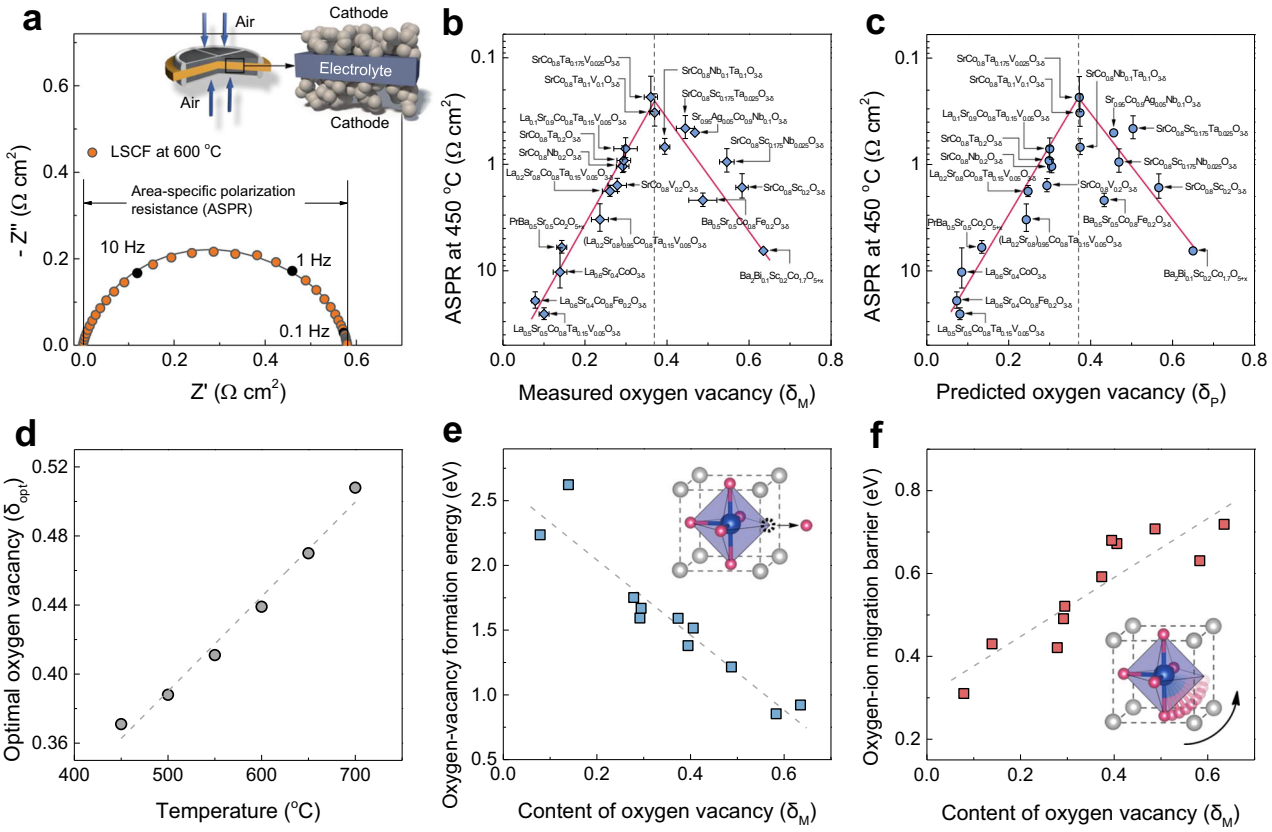


Fig. 2 | Correlation between the concentration of oxygen vacancy and ORR activity of cobalt-based perovskite oxides. a Illustration of how area polarization resistance (ASPR) is determined from Nyquist plot over LSCF cathode at 600 °C in a symmetric cell configuration shown in the inset schematics. **b**, **c** The ORR activity (mean values ± S.D.) at 450 °C as a function of the (**b**) measured (mean values ± S.D.) and (**c**) ML-predicted oxygen vacancy concentration. The measurements of δ_M and ASPRs were repeated for three times. **d** The evolution of the optimal oxygen vacancies for ORR activity as a function of operating temperatures. **e**, **f** Comparison of DFT-calculated (**e**) formation and (**f**) mobility of the oxygen vacancy in the perovskite lattice.

dominant contribution of oxygen vacancies to the oxygen-reduction catalytic activity at elevated temperatures. The catalytic activities of the perovskite materials are commonly evaluated at the symmetrical cells, as illustrated in Fig. 2a, where the targeted materials are deposited on both sides of dense electrolyte disks, such as gadolinium-doped ceria (GDC). The activity is described by the area-specific polarization resistance (ASPR) determined from the Nyquist plot shown in Fig. 2a. A low ASPR value indicates a high ORR activity.

As compared to room temperature electrocatalysis, the elevated temperature electrocatalysis is more complicated, because the electrocatalyst should be fabricated into porous electrodes. The measured ASPR value for elevated temperature electrocatalysis is not only a result of the material's intrinsic activity but also affected by the electrode microstructures, the electrode-electrolyte interface, and the operating conditions (*e.g.*, temperatures and oxygen partial pressures). Consequently, the reported ASPR values of the same electrode material could vary vastly when tested by different research groups (see examples in Supplementary Fig. S7), similar to the results obtained from Jacobs et al[49]. Such large variations make it challenging to directly compare the reported activity in the literature. Therefore, instead of comparing reported activity from other labs, we synthesized 19 cobalt-based perovskite oxides and tested their ORR activity on the symmetrical cells following the same protocol, so as to study the intrinsic activity of the materials. The samples for the test include 12 reported perovskite oxides[8,12,15,39,50–57] and 7 new oxides, including $SrCo_{0.8}V_{0.2}O_{3-\delta}$, $SrCo_{0.8}Ta_xV_{0.2-x}O_{3-\delta}$ (x = 0.1 and 0.175), $La_ySr_{1-y}Ta_{0.15}V_{0.05}Co_{0.8}O_{3-\delta}$ (y = 0.10, 0.20 and 0. 50), and $(La_{0.2}Sr_{0.8})_{0.95}Ta_{0.15}V_{0.05}Co_{0.8}O_{3-\delta}$. The X-ray diffraction (XRD) analysis show that our perovskite oxides are mainly in $Pm\bar{3}m$ cubic structure, with lattice parameters similar to those of reported perovskites (Supplementary Fig. S8 and Table S1). The fabricated cathodes for the symmetrical cells are in similar cathode microstructures (Supplementary Fig. S9 and Fig. S10).

Figure 2b, c show the trend of the ASPR values of the model materials as a function of the predicted and tested concentration of oxygen vacancies, respectively. The measured oxygen vacancies are linearly correlated with the predicted ones (Supplementary Fig. S11). We experimentally determined the concentration of oxygen vacancies via a typical chemical titration method for oxygen vacancy estimation at room temperature cases and thermogravimetric analysis for different temperatures (Supplementary Fig. S12). The temperature-programmed desorption mass spectrometry (TPD-MS) shows no peak relevant to CO_2 or water at temperatures above 300 °C (Supplementary Fig. S13), illustrating that the oxygen vacancy formation is the main result of the mass loss. The results are consistent with those obtained by using Co-K edge X-ray absorption near-edge spectroscopy (XANES) method (Supplementary Fig. S14). The results unveil a strong volcano correlation, where the catalytic activity varies with the concentration of oxygen vacancies to a degree of over three orders of magnitude. Such a trend implies the dominant role of the oxygen vacancies in predetermining the oxygen reduction activity.

Although the electron conductivity is also a prerequisite for the cathode for current collection, it seems not the dominating factor for the ORR activity as compared to the concentration of the oxygen vacancies (Supplementary Fig. S15). This observation can be reasonably explained by the much higher electronic conductivity than oxygen ion conductivity at elevated temperatures of perovskite oxides.

Interestingly, we also noticed that an easy formation of oxygen vacancies in the metal oxides does not always lead to improved activity. The high-performance perovskites usually contain a moderate level of oxygen vacancies (e.g., $\delta = 0.2–0.45$ for cobalt-based materials at 450 °C). This general relation reflects what we frequently observed in recent cathode development: the $NdBaCo_2O_{5+x}$[58], $PrBaCo_{1.9}Sc_{0.1}O_{5+x}$[59], and $SrNb_{0.1}Co_{0.8}Fe_{0.2}O_{3-\delta}$[60] with $\delta = 0.2 - 0.45$ show superior ORR activity to the BSCF, $SrSc_{0.2}Co_{0.8}O_{3-\delta}$ (SSC) and $Ba_2Bi_{0.1}Sc_{0.2}Co_{1.7}O_{5+x}$[51] with $\delta = 0.45 - 0.64$ at the right branch and the ones (e.g., $La_{0.6}Sr_{0.4}Co_{0.8}Fe_{0.2}O_{3-\delta}$ (LSCF), $PrBa_{0.5}Sr_{0.5}Co_2O_{5+x}$ (PBSC) with $\delta = 0.08 - 0.15$) lying at the left.

Further, the top region of the volcano varies with the operating temperatures. The concentration of the oxygen vacancy for optimal oxygen reduction increases from 0.375 at 450 °C to 0.508 at 700 °C (Fig. 2d), suggesting the enhanced oxygen vacancy participation within the oxygen electrocatalysis with the increase of operation temperature, as expected. Synchronously, the optimal oxides for catalysis change from $SrCo_{0.8}Ta_{0.175}V_{0.025}O_{3-\delta}$ (SCTV0.175) at below 500 °C to SCTV0.175 and $SrSc_{0.175}Ta_{0.025}Co_{0.8}O_{3-\delta}$ (SSTC) at 500-600 °C, and then to SSTC at 700 °C. This temperature dependency might also pose significant challenges for one to identify the optimal catalyst candidates for high-temperature operations purely from theoretical calculations. This issue is originated from the prerequisite of the theoretical models for the precise states of the redox-active metals such as cobalt at a specified temperature, which can usually be determined through time-consuming in-situ measurements and analyses[61,62]. Therefore, this step, together with the identified temperature dependency in this study, hinders a quick exploration of the material space for high-temperature catalysis.

The role of oxygen vacancies in determining catalytic activity

To obtain a deeper understanding of the role of oxygen vacancies in the catalytic activity, we then calculated the energies of oxygen vacancy formation and migration from DFT calculations. Details of the calculation are described in Methods and Supplementary Figs. S16-S19. The simulation results, shown in Fig. 2e, imply that the materials with low oxygen vacancy formation energies can create oxygen vacancies easily. By contrast, the oxygen-ion migration is slow within the materials containing a high concentration of oxygen vacancies (Fig. 2f). We believe the inverse trend between oxygen vacancy formation and mobility is likely related to the ionic character of the cobalt-oxygen bonds. Although an increase in electron density close to cobalt promotes oxygen vacancy formation, it reduces the ionic character of the bonds and then slows down the oxygen-ion migration by weakening the electrostatic attraction between negatively charged oxygen ions and their neighboring positively charged oxygen vacancies[63,64].

Further, the simulation results allow us to explain the volcano dependency of the ORR activity over oxygen vacancy. The right branches of the volcano trend are essentially controlled by the oxygen-ion mobility in the lattice. With the high oxygen-ion mobility but low concentration of oxygen vacancy, on the other hand, the left branches of the volcano are controlled by oxygen vacancy concentration. The top of the volcano is the region with an optimal balance between oxygen vacancy formation and oxygen-ion mobility, which is desired for efficient oxygen reduction catalysis. However, the models are limited to elucidating the observed temperature dependency of the optimal perovskite oxides for catalysis. We envisage such temperature dependence is likely a result of different levels of participation of the thermally activated material bulk ionic transport and surface exchange in the catalysis process.

Rational design of ORR electrocatalysts for solid oxide fuel cells

The strong activity–oxygen vacancy correlation offers new opportunities to guide the design of new metal oxides for catalysis at different temperatures. To prove the concept of rational material design based on the identified activity-oxygen vacancy correction and prediction of oxygen vacancies from a lattice cationic environment, we take the development of cathode materials for low-temperature solid oxide fuel cells (SOFCs) as an example.

Figure 3a describes the flow chart to design high-performance cathode materials using $SrCoO_{3-\delta}$ (SC) as the model parent oxide. We chose SC based oxides as the model perovskites to prove our concept because they represent one of the most active candidates for ORR, such as BSCF, LSCF, SSC, and $SrCo_{0.8}Nb_{0.1}Ta_{0.1}O_{3-\delta}$ (SCNT). The first step is to apply the machine learning model to predict the concentration of the oxygen vacancies of the targeted compositions. An ideal SC-based cathode composition should lead to a cubic structure (with a tolerance factor close to unity) and a moderate level of oxygen vacancies at elevated temperatures. The second step is experimental verification, which includes material synthesis, characterization, cathode fabrication, and activity evaluation.

From this ML-assisted process, we identified two new perovskite oxides, $SrCo_{0.8}Ta_{0.16}W_{0.04}O_{3-\delta}$ (SCTW) and $SrCo_{0.8}Ta_{0.15}V_{0.05}O_{3-\delta}$ (SCTV), which could meet the criteria as good cathode materials for SOFC operated at below 500 °C. Both materials show tolerance factors close to unity, indicating the potential formation of cubic structure phases. The oxygen vacancy concentration is predicted to be 0.317 for SCTW and 0.356 for SCTV at 450 °C, which are close to the optimal oxygen vacancy concentration for ORR at this temperature since they are located at the top of the volcano as shown in Fig. 3b, c. The two examples with uncommon dopants at B-sites (e.g., W and V) are proposed to support the validity of the ML-assisted prediction process to design catalysts that are beyond conventional compositions.

We experimentally synthesized SCTW and SCTV materials and verified their crystal structure using Rietveld analysis of XRD (Supplementary Fig. S20), with details shown in Supplementary Table S2 and Table S3. The results reveal that both SCTV and SCTW are in $Pm\bar{3}m$ space group. The lattice parameters are 3.8916(5) for SCTV and 3.8969(2) for SCTW, consistent with the larger size of W^{5+} and Ta^{5+} compared to V^{5+}[33]. Besides, the concentrations of oxygen vacancies of both perovskites, determined by using the chemical titration method at room temperature, are in consistence with our predictions based on machine learning (Supplementary Fig. S21). We then fabricated the cathodes with the targeted composition and experimentally tested their oxygen vacancy concentration and ORR activity as a function of temperature. As shown in Fig. 3b, c, both tested cathode materials exhibited very similar concentrations of oxygen vacancies to the predicted values from our models across a wide temperature range. This result further validates the effectiveness of the ML model and local cationic environment in predicting oxygen vacancy with minimal computation power. When applied as ORR electrocatalysts based on the symmetrical cells, both perovskite materials showed unprecedented activity at reduced temperatures with the ASPR of $0.265 \pm 0.041\ \Omega\ cm^{-2}$ for SCTW and $0.165 \pm 0.067\ \Omega\ cm^2$ for SCTV at 450 °C. These two electrode materials are superior to all the state-of-the-art ORR electrodes (e.g., LSCF, BSCF, PBSC, SSNC, and SCNT) at reduced operating temperatures tested under the same conditions (Fig. 3d and Supplementary Table S4).

We then applied SCTV as the cathode for three solid oxide single cells for power generation from hydrogen gas. The cells for the test are anode-supported in a configuration of the SCTV (~18 μm) | GDC (13–18 μm) | Ni-GDC (~700 μm) (Fig. 4a, b). As enabled by the ORR-active electrocatalyst, as shown in Fig. 4c and Supplementary Fig. S22, all three cells achieved peak power densities (PPDs) above $0.6\ W\ cm^{-2}$ at 450 °C. For example, the Cell-1 shown in Fig. 4c achieved a PPD as high as $1.36\ W\ cm^{-2}$ at 500 °C, $0.85\ W\ cm^{-2}$ at 450 °C, and $0.45\ W\ cm^{-2}$ at 400 °C, surpassing most of the reported performance of single cells operated below 500 °C (Supplementary Table S5).

We also evaluated the short-term stability of Cell-1 and Cell-2. Under a constant current density of $0.272\ A\ cm^{-2}$, as shown in Fig. 4h

https://doi.org/10.1038/s41467-024-53578-7

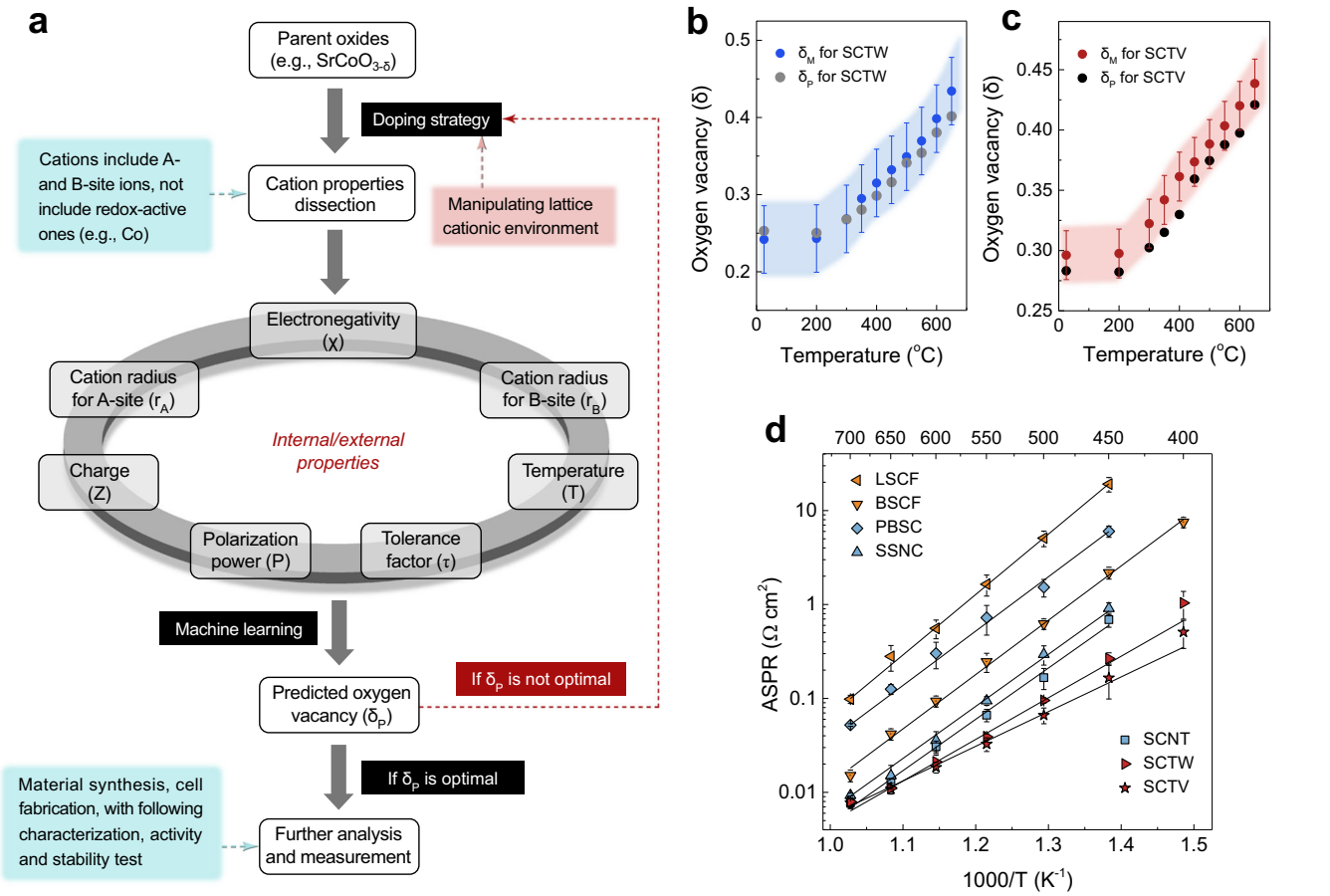


Fig. 3 | ML-assisted catalyst design and ORR performance verification. a Flow chart of proposed ML-assisted rational design of perovskite catalysts for fuel cells. **b**, **c** Comparisons of ML predicted oxygen vacancy (δ_P) with mean values ± S.D. of measured oxygen vacancy (δ_M) for two designed catalysts of (**b**) $SrCo_{0.8}Ta_{0.16}W_{0.04}O_{3-\delta}$ (SCTW) and (c) $SrCo_{0.8}Ta_{0.15}V_{0.05}O_{3-\delta}$ (SCTV). **d** Mean values ± S.D. of ASPRs for selected perovskite oxides in the electrode (~10 μm) | electrolyte | electrode (~10 μm) symmetrical cell configurations tested in 100 ml min^{-1} air at 400–700 °C. The measurements of δ_M and ASPRs were repeated for three times.

and Supplementary Fig. S23, Cell-1 showed a degradation rate of 47.7 mV/1000 h for the 600 h range and 18.3 mV/1000 h for the last 350 h at 375 °C. Such degradation, especially at the first 250 h, is likely related to the sealing issue after thermal cycling (Supplementary Fig. S24) and the susceptibility of the cathode to the CO_2 in the ambient air (Supplementary Fig. S25). In contrast, Cell-2 did not undergo thermal cycling and thus achieved better durability with negligible degradation for the first 210 h operation at 0.272 A cm^{-2} at 500 °C. Although the SCTV is not completely resistant to 1 % CO_2 due to the presence of Sr, it still shows a much better CO_2 tolerance than the benchmark BSCF cathode (Supplementary Fig. S26 and Fig. S27) and is expected to be further improved by strategies such as altering A-site cations[65] or compositing cathodes with electrolytes[53,66].

In summary, this work reports an alternative approach to predict one of the most important properties of perovskite oxides—concentration of oxygen vacancies—across a wide range of temperatures without the requirement for heavy theoretical computation. Our results reveal that the successful prediction of the oxygen vacancy concentrations arises from the important role of the lattice cationic environment in determining the formation of oxygen vacancies and the commonly existing delocalized electron distribution over the active metal centres of the perovskite materials, such as cobalt and iron.

Based on the prediction of oxygen vacancies, a new approach is proposed to guide the design of perovskite materials for oxygen electrocatalysis at different temperatures, where the concentration of oxygen vacancies predetermines the intrinsic activity. Meanwhile, we discovered two new perovskite oxides that show unprecedented activity to reduce oxygen at below 500 °C, enabling sufficient power generation from solid oxide fuel cells at below 500 °C. Our findings are anticipated to contribute to the advancement of materials for key applications where oxygen vacancies play a vital role, such as fuel cells, electrolysis, energy storage, thermal catalysis, and random-access memory.

Discussion

Our findings are anticipated to be effective in guiding new material development for other applications operated at a wide range of temperatures, if there is a strong performance-oxygen vacancy relationship, including solid oxide electrolysis for hydrogen production[67], CO_2 electrolysis[2], thermochemical catalysis[68], oxygen storage or pumping[69], thermal energy storage[70], and ferroelectric random-access memory[71]. The two typical examples (water oxidation at room temperature and SOFC at high temperatures) discussed in this study imply that the optimal concentration of the oxygen vacancies varies with the applications and the catalyst operating temperatures. Bearing such variations in mind, we envision that the performance-oxygen vacancy relationship could serve as a new avenue for researchers to explore, so as to achieve an effective prediction of the material performance. Therefore, the prediction toolkit reported in this study could also help

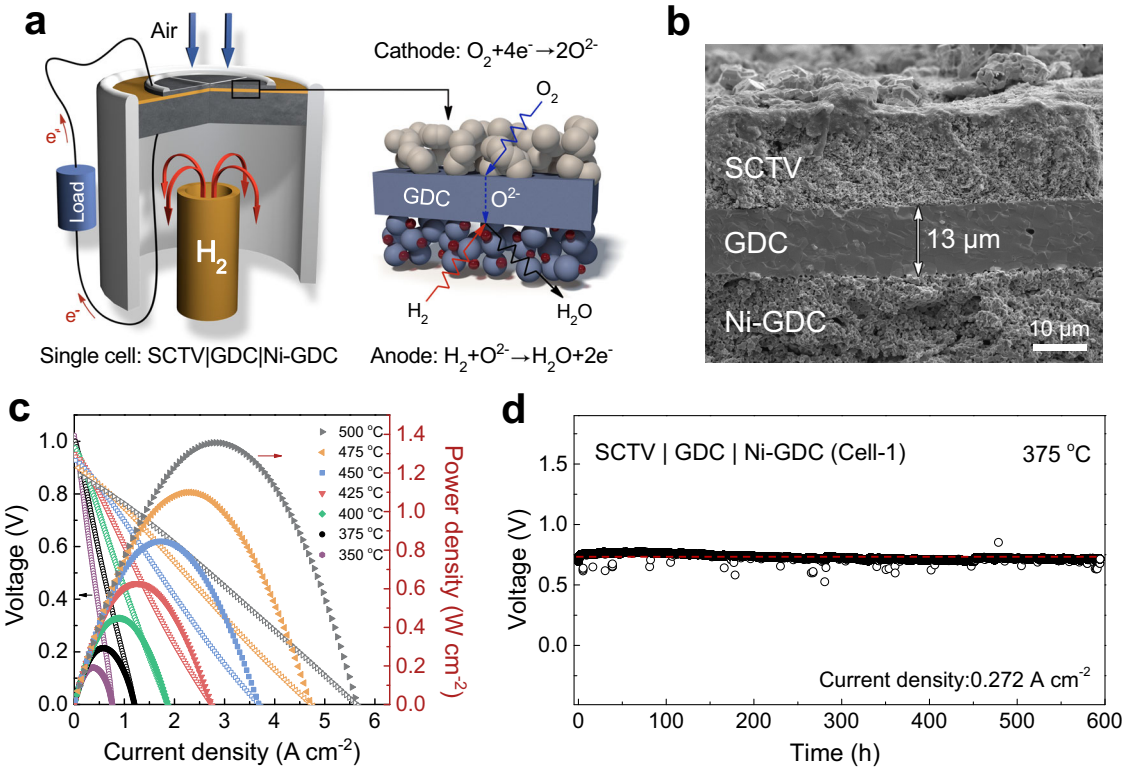


Fig. 4 | Power density and stability of solid oxide fuel cells using SCTV as the cathode. a An illustration of an anode-supported solid oxide single cell. **b** Scanning electron micrograph of the cross-section of the tested single cell using SCTV as the cathode. **c** Voltage-current density curves and power densities of the tested Cell-1 across different operating temperatures. **d** Short-term stability test of Cell-1 operated at 375 °C at a constant current density of 0.272 A cm^{-2}. In these single-cell tests, 80 ml min^{-1} H_2 was supplied to the anode, and 120 ml min^{-1} air was supplied to the cathode.

accelerate such a process, which has been demonstrated by our case in SOFC cathode development.

Although our new approach provides an alternative tool for researchers to explore the compositional space of the materials, it is also important to note that other non-compositional factors could not be overlooked when determining the overall performance of the materials, such as the particle sizes[48], dimensionality (i.e., 2D materials)[72], microstructures[73,74], interfaces[75], and local reaction environment[76]. Additionally, the accuracy of the prediction can be affected by the size and quality of the learning dataset. Besides, this work relies on comprehensive existing datasets for model training and predictions. Due to the limited data available in the literature for other metal-based perovskite oxides, the models reported here are only valid for predicting cobalt- or iron-based perovskite oxides at different temperatures. Hence, these non-compositional factors, as well as large datasets with high quality, are also highly desired in future efforts and serve as inputs for the data training processes, which is expected to further improve the accuracy of the activity prediction and accelerate the paradigm shift towards the more efficient rational material design than the conventional trial-and-error approaches.

Methods

Machine learning

We derived a Python-based machine learning (ML) toolbox for automatically predicting oxygen vacancies of Co-based and Fe-based perovskites. Forty-one ML models were optimized and evaluated by five-fold cross-validation on the test set and were ranked by the R-squared scores for model selection. Amongst all compared regression models, ensemble methods have demonstrated a better generalization performance on the test set by combining the predictions of several base estimators. Representative ensemble methods can be categorized into averaging methods, e.g., extremely randomized trees/extra-trees[77] (ExtraTreesRegressor), random forests[78] (RandomForestsRegressor), and boosting methods, e.g., Adaboost[79] (AdaBoostRegressor), gradient boosting[80] (GradientBoostingRegressor). As the LGBMRegressor model achieved one of the best performances, we chose it to establish the final predictive model and studied the learning curves and the partial dependence.

Materials preparation

The solid-state synthesis method[81] was applied to synthesize the perovskite-type oxides of $SrCo_{0.8}V_{0.2}O_{3-\delta}$ (SCV), $SrCo_{0.8}Nb_{0.2}O_{3-\delta}$ (SCN), $SrCo_{0.8}Ta_{0.2}O_{3-\delta}$ (SCT), $SrSc_{0.2}Co_{0.8}O_{3-\delta}$ (SSC), $SrSc_{0.175}Nb_{0.025}Co_{0.8}O_{3-\delta}$ (SSNC), $SrSc_{0.175}Ta_{0.025}Co_{0.8}O_{3-\delta}$ (SSTC), $SrCo_{0.8}Ta_xV_{0.2-x}O_{3-\delta}$ (x = 0.10 and 0.175), $SrCo_{0.8}Nb_{0.1}Ta_{0.1}O_{3-\delta}$ (SCNT), $La_ySr_{1-y}Co_{0.8}Ta_{0.15}V_{0.05}O_{3-\delta}$ (y = 0.1, 0.2 and 0.5), $(La_{0.2}Sr_{0.8})_{0.95}Ta_{0.15}V_{0.05}Co_{0.8}O_{3-\delta}$, $SrCo_{0.8}Ta_{0.16}W_{0.04}O_{3-\delta}$ (SCTW), and $SrCo_{0.8}Ta_{0.15}V_{0.05}O_{3-\delta}$ (SCTV). Taking SCTV as an example, the stoichiometric mixtures of $SrCO_3$ (Sigma, ≥ 99.9 %), Co_3O_4 (Sigma, ≥ 99.5 %), V_2O_5 (Sigma, ≥ 99.6 %) and Ta_2O_5 (Alfa Aesar, ≥ 99.0 %) were ball-milled at 260 rpm for 20 h, dry-pressed in a die under ~180 MPa and then sintered at 1200 °C for 20 h. The sintered tablets were crushed into powders via ball-milling at 300 rpm for 6 h.

$Ba_{0.5}Sr_{0.5}Co_{0.8}Fe_{0.2}O_{3-\delta}$ (BSCF), $La_{0.6}Sr_{0.4}Co_{0.8}Fe_{0.2}O_{3-\delta}$ (LSCF), $La_{0.6}Sr_{0.4}CoO_{3-\delta}$ (LSC), and $PrBa_{0.5}Sr_{0.5}Co_2O_{5+x}$ (PBSC) were synthesized by the sol-gel method. Taking BSCF as an example, the stoichiometric mixtures of $Ba(NO_3)_2$ (Sigma, ≥ 99.0 %), $Sr(NO_3)_2$ (Sigma, ≥ 99.0 %), $Co(NO_3)_2{\cdot}6H_2O$ (Sigma, ≥ 99.0 %) and $Fe(NO_3)_3{\cdot}9H_2O$ (Sigma, ≥ 99.95 %) were dissolved into de-ionized water with vigorous stirring until a transparent solution was formed, followed by addition

of known mass of citric acid (Sigma, ≥ 99.5 %) and ammonia-dissolved ethylenediaminetetraacetic acid (EDTA, Sigma, ≥ 99.0 %). The molar ratio of metal nitrates, citric acid, and EDTA was 1:1.5:2.0, and the pH value of the mixed solution was adjusted to 9–10 by ammonia (Alfa Aesar, 28–30 %). After evaporation of water at 80 °C for 12 h, a viscous gel was obtained. The gel was then pre-calcined at 250 °C for 3 h to obtain the pristine powder, which was subsequently calcined at 950 °C for 5 h in the air to form BSCF powder.

Materials characterization

Scanning electron microscopic images (SEM, JEOL JSM-7001F) was applied at 15 kV to investigate the thickness of perovskite materials on electrolyte. The crystal structure of the materials was verified from X-ray diffraction (XRD, Bruker D8) on a Philips X'pert Pro Super diffractometer with a radiation source of Cu-K_α ($\lambda = 1.5418$ Å) at a voltage of 40 kV and a current of 40 mA. Thermogravimetric (TG, Perkin Elmer STA6000) analysis was conducted to reveal the weight loss of the materials during heating from room temperature to 800 °C in air. Iodometric titration was used to determine the oxygen non-stoichiometry (δ) in the material. X-ray absorption spectra (XAS) were recorded to investigate the bulk characteristics of the materials on the wiggler XAS beamline (12 ID) at Australian Synchrotron (AS), with a beam energy of 3.0 GeV and a maximum beam current of 400 mA. Nano Measurer software was used to determine the size of sintered perovskite particles on electrolyte.

Electrical conductivity of the perovskite oxides

The perovskite powders were pressed and then sintered at 1200 °C for 5 h to form dense bars. The relative densities of the samples were over 95 %. After polish, the silver wires were attached to the sample bars, followed by the electrical conductivity by using a DC 4-probe method on Autolab PGSTAT 302 N. To ensure the accuracy, the measurements were conducted in the presence of flow air (120 mL min^{-1}). All measurements were repeated for three times.

Oxygen evolution reaction (OER) measurements of the perovskite oxides

10 mg perovskite powder was ultrasonically mixed with 10 mg carbon black (Super C65, TIMCAL C'NERGY) in 1.0 mL ethanol with 100 µL Nafion™ 117 solution (Sigma, 5 wt.% in ethanol) for 40 min. Then, 5 µL suspension was drop-cast onto a glassy carbon disk electrode (diameter of 5.0 mm, area of 0.196 cm^2, mass loading of 0.045 mg) and dried in a vacuum oven at room temperature. The Pt wire was used as the counter electrode and an Hg/HgO electrode was used as the reference electrode. The electrochemical cyclic voltammograms (CV) measurements (0-0.9 V vs Hg/HgO) of the perovskite materials were conducted in 0.1 M KOH (Sigma, stored at room temperature without contacting air, saturated with 99.999 % O_2 before usage) at a scan rate of 5 mV s^{-1} at room temperature by using a rotating disk electrode (RDE) device. The data were collected after the stabilization of CV curves. The potentials tested in this work are *iR*-corrected according to the following equation:

$$E(RHE) = E(Hg/HgO) + 0.110V + 0.059 \times pH - 90\,\% \times iR \quad (2)$$

where i and R represent current and ohmic resistance of 0.1 M KOH, respectively, and E(Hg/HgO) is the measured potentials. All measurements were repeated for three times.

Calculation of oxygen vacancy at room temperature

Iodometric titration was applied to determine the oxygen vacancy in the perovskite-type oxides[82]. Generally, 0.1 g pre-dried oxide was mixed with 2.0 g KI (Sigma, ≥ 99.0 %) in an Erlenmeyer flask, followed by sealing with Ar gas (99.999 %) for 10 min and adding 10 mL HCl (3.0 mol L^{-1}). The ultrasound treatment was applied to better dissolve the oxide in HCl acid. The solution was then titrated with 0.1 mol L^{-1} $Na_2S_2O_3$ (Sigma, 99.99 %).

Taking $SrCo_{0.8}Nb_{0.1}Ta_{0.1}O_{3-\delta}$ (SCNT) oxide as an example, only Co ion participates in the redox reaction. The oxidation state of Co is assumed as +x, and the redox reactions during the titration can be expressed as:

$$Co^{x+} + (x-2)I^- = Co^{2+} + \frac{x-2}{2} I_2 \quad (3)$$

$$I_2 + 2Na_2S_2O_3 = 2NaI + 2Na_2S_4O_6 \quad (4)$$

So that the stoichiometric relationship between SCNT and $Na_2S_2O_3$ should be:

$$SrCo_{0.8}Nb_{0.1}Ta_{0.1}O_{3-\delta} \sim \frac{x-2}{2} \times 0.8 I_2 \sim (x-2) \times 0.8 Na_2S_2O_3 \quad (5)$$

The molar relationship between SCNT and $Na_2S_2O_3$ is calculated as:

$$\frac{m}{M} \times 0.8 \times (x-2) = cV \quad (6)$$

where m and M are the exact mass and molar mass of SCNT cathode, while c and V represent the concentration and volume of the $Na_2S_2O_3$ solution. The presence of oxygen vacancy will inevitably lead to a decrease in oxygen non-stoichiometry δ_O at room temperature. So that M can be expressed as:

$$M = M_{Sr} + M_{Nb} \times 0.1 + M_{Ta} \times 0.1 + M_{Co} \times 0.8 + M_O \times (3 - \delta_0) \quad (7)$$

where M_{Sr}, M_{Nb}, M_{Ta}, M_{Co}, and M_O represent the molar atomic mass of Sr, Nb, Ta, Co, and O, being 87.62, 92.91, 180.95, 58.93, and 16.00 g mol^{-1}, respectively.

Besides, the conservation of charge in SCNT can provide another equation:

$$X_{Sr} + X_{Nb} \times 0.1 + X_{Ta} \times 0.1 + X_{Co} \times 0.5 = X_O \times (3 - \delta_0) \quad (8)$$

where X_{Sr}, X_{Nb}, X_{Ta}, X_{Co}, and X_O are the valences of Sr, Nb, Ta, Co, and O, being +2, +5, +5, +x, and −2, respectively.

In summary, the oxygen non-stoichiometry of δ_O can be calculated from the association of Eq. (6)—Eq. (8). All titration measurements were repeated for three times.

Calculation of oxygen vacancy at elevated temperature

Thermogravimetric (TG) analysis was performed to weigh the mass loss of sample at 150-800 °C, and thus calculate the δ_T at elevated temperature. To eliminate the moisture in the sample, efforts were made to maintain the temperature at 150–200 °C for 1.5 h. Assuming that no oxygen vacancy exists in the SCNT material, the original mass of the sample should be:

$$m_{original} = \frac{m \times (M + M_O \times \delta_0)}{M} \quad (9)$$

where M is the molar mass of SCNT, and M_O represents the molar atomic mass of the oxygen atom. So that the SCNT mole ($M_{original}$) can be calculated from Eq. (10), no matter how much oxygen goes away as the raising of temperature.

$$M_{original} = \frac{m_{original}}{M + M_O \times \delta_0} \quad (10)$$

Then the δ_T will be obtained from:

$$\delta_T = \frac{(m_{original} - m_T)/M_O}{M_{original}} \quad (11)$$

where m_T is the sample mass at temperature T.

Preparation of symmetrical and single cells

The symmetrical cells with configuration of perovskite | $Gd_{0.1}Ce_{0.9}O_{1.95}$ (GDC, 10–14 $m^2 \cdot g^{-1}$, purchased from Single Cell Materials) | perovskite were fabricated for electrochemical impedance spectroscopy (EIS) analysis. The GDC powder was pressed in a die under ~90 MPa, followed by sintering at 1450 °C for 5 h to form dense electrolyte disks with a single-side area of ~1.1 cm^2 and thickness of ~0.7 mm. The cathode slurry was prepared by ball-milling 6.0 g fresh perovskite oxides with 0.3 g dispersant (20 wt.% vegetable oil dispersed in terpinol) and 0.1 g binder (20 wt.% ethylcellulose dispersed in terpinol) in 60 g isopropanol. The as-prepared cathode slurry was then sprayed evenly on both sides of the GDC electrolyte disks with an N_2-borne spray gun, followed by calcination at 950 °C for 2 h. The symmetrical cells, stored in air at room temperature, were then assembled by grafting a silver electrode using silver paste on both sides of the cathode-covered GDC disk, with a thin silver paste painted on the surface of the cathode to better collect electrons.

The SCTV-based single cell with the SCTV (cathode) | GDC (electrolyte) | NiO-GDC (anode) structure was prepared to investigate the electrochemical performance of perovskite-type cathode in a lab-scale SOFC device. The anode precursor of NiO-GDC was obtained by ball-milling the mixtures of NiO (Sigma, 99.99 %), GDC, dextrin (Sigma), and graphite (Sigma, < 20 μm) with a mass ratio of 6:4:0.6:0.4 in ethanol for 24 h. After drying at 150 °C for 2 h, the NiO-GDC substrate powder was co-pressed with GDC power under ~180 MPa into button-like pellets, followed by the calcination at 1450 °C for 7 h. The thickness of the GDC electrolyte layer was 13–18 μm. The cathode slurry was subsequently sprayed onto the GDC side with an area of 0.24 cm^2, followed by calcination at 950 °C for 2 h to obtain single cells. The prepared single cells were store in air at room temperature. The thickness of the cathode layer was 10–20 μm. After adhering silver lines to both the cathode and anode sides, the silver paste was then applied as a high-temperature sealant to seal single cells on alumina tubes.

Cell characterization

The performance of symmetrical and single cells was measured on Autolab PGSTAT 302 N. The EIS analysis of symmetrical cells was performed at 400–700 °C in flowing air (300 mL·min^{-1}). The frequency range and signal amplitudes were 0.1–100 kHz and 10 mV, respectively. For fuel cells, the current-voltage curves were tested at 350–500 °C with H_2 on the anode side (80 mL·min^{-1}) and air on the cathode side (120 mL·min^{-1}). The signal amplitude was 10 mV, and the frequency range was 0.1–100 kHz. The stability tests were conducted at 375 °C and 500 °C at 0.272 A cm^{-2}, with H_2 flow of 80 ml min^{-1} on the anode side and air flow of 120 ml min^{-1} on the cathode side. All measurements were repeated for three times.

Density functional theory (DFT) calculations

Density functional theory as implemented in the Vienna Ab-initio Simulation Package (VASP) with the projector augmented waves methods was employed to relax the unit cells and optimize structures[83–85]. The generalized gradient approximation (GGA) with the PBEsol method was performed to describe the exchange-correlation[86]. For transition metal 3d electrons, the GGA + U calculations were used with the simplified spherically-averaged approach, and U_{eff} ($U_{eff} = U_{coulomb} - J_{exchange}$) was set to 0.80 eV, according to the previous references[12]. Long-range van der Waals dispersion was also considered in this calculation by using empirical correction in Grimme's scheme[87]. Cut-off energy of 520 eV for plain-weave basis sets was adopted and the convergence threshold was 10^{-5} eV, and 5×10^{-3} eV/Å for energy and force, respectively. To mimic the real experimental condition, the cubic $SrCoO_3$ models were established by substituting Co atoms with co-dopants to form supercells with scales of 2 × 2 × 2 (e.g., for $SrCo_{0.8}Nb_{0.2}O_{3-\delta}$, $La_{0.6}Sr_{0.4}CoO_{3-\delta}$, and $Ba_{0.5}Sr_{0.5}Co_{0.8}Fe_{0.2}O_{3-\delta}$) and 2 × 2 × 4 (e.g., for $SrCo_{0.8}Ta_{0.1}V_{0.1}O_{3-\delta}$, $SrSc_{0.175}Nb_{0.025}Co_{0.8}O_{3-\delta}$, and $SrCo_{0.8}Nb_{0.1}Ta_{0.1}O_{3-\delta}$), and a 3 × 3 × 3 Monkhorse-pace mesh was chosen for k-sampling of the Brillouin zone. The climbing nudged elastic band method was employed to search the saddle points and minimum energy pathways[88,89]. The formation energies of an oxygen vacancy (E_f) in perovskite structures were calculated by the following equation:

$$E_f = E_{vacancy} - E_{pristine} + \frac{1}{2}E_{O_2} \quad (12)$$

where $E_{vacancy}$ and $E_{pristine}$ represent the total energies of the lattice structures without and with oxygen vacancy, while E_{O2} is the oxygen energy that has departed from the perovskite model.

Data availability

Source data are provided with this paper.

Code availability

The codes for machine learning in this study are available at *Zhiheng Li, Xin Mao, Desheng Feng, Mengran Li, Xiaoyong Xu, Yadan Luo, Linzhou Zhuang, Rijia Lin, Tianjiu Zhu, Fengli Liang, Zi Huang, Dong Liu, Zifeng Yan, Aijun Du, Zongping Shao, Zhonghua Zhu, Prediction of Perovskite Oxygen Vacancies for Oxygen Electrocatalysis at Different Temperatures, mengranli/MLtoolbox-perovskite-oxygen-vacancy-pred: POV 1.0.0 (PerovskiteOxide). Zenodo*. https://doi.org/10.5281/zenodo.13932503, *2024*.

References

1. Sun, W. et al. A rechargeable zinc-air battery based on zinc peroxide chemistry. *Science* **371**, 46–51 (2021).
2. Huang, J. E. et al. CO_2 electrolysis to multicarbon products in strong acid. *Science* **372**, 1074-–1078 (2021).
3. Oener, S. Z., Foster, M. J. & Boettcher, S. W. Accelerating water dissociation in bipolar membranes and for electrocatalysis. *Science* **369**, 1099–1103 (2020).
4. Chen, Y. et al. A robust fuel cell operated on nearly dry methane at 500 °C enabled by synergistic thermal catalysis and electrocatalysis. *Nat. Energy* **3**, 1042–1050 (2018).
5. Jiao, K. et al. Designing the next generation of proton-exchange membrane fuel cells. *Nature* **595**, 361–369 (2021).
6. Chong, L. et al. La- and Mn-doped cobalt spinel oxygen evolution catalyst for proton exchange membrane electrolysis. *Science* **380**, 609–616 (2023).
7. Huang, H. et al. Clusters induced electron redistribution to tune oxygen reduction activity of transition metal single-atom for metal–air batteries. *Angew. Chem.* **134**, e202116068 (2022).
8. Shao, Z. P. & Haile, S. M. A high-performance cathode for the next generation of solid-oxide fuel cells. *Nature* **431**, 170–173 (2004).
9. Hauch, A. et al. Recent advances in solid oxide cell technology for electrolysis. *Science* **370**, eaba6118 (2020).
10. Mefford, J. T. et al. Water electrolysis on $La_{1-x}Sr_xCoO_{3-\delta}$ perovskite electrocatalysts. *Nat. Commun.* **7**, 11053 (2016).
11. Suntivich, J. et al. Design principles for oxygen-reduction activity on perovskite oxide catalysts for fuel cells and metal–air batteries. *Nat. Chem.* **3**, 546–550 (2011).
12. Li, M. R. et al. A niobium and tantalum co-doped perovskite cathode for solid oxide fuel cells operating below 500 °C. *Nat. Commun.* **8**, 13990 (2017).

13. Zheng, Y., Chen, Z. & Zhang, J. Solid oxide electrolysis of H_2O and CO_2 to produce hydrogen and low-carbon fuels. *Electrochem. Energy R.* **4**, 508–517 (2021).
14. Li, Z., Li, M. & Zhu, Z. Perovskite cathode materials for low-temperature solid oxide fuel cells: fundamentals to optimization. Electrochem. *Energy Rev.*, **5**, 263–311 (2021).
15. Zhou, W. et al. A highly active perovskite electrode for the oxygen reduction reaction below 600 °C. *Angew. Chem. Int. Ed.* **52**, 14036–14040 (2013).
16. Xia, C. et al. Shaping triple-conducting semiconductor $BaCo_{0.4}Fe_{0.4}Zr_{0.1}Y_{0.1}O_{3-\delta}$ into an electrolyte for low-temperature solid oxide fuel cells. *Nat. Commun.* **10**, 1707 (2019).
17. Sengodan, S. et al. Layered oxygen-deficient double perovskite as an efficient and stable anode for direct hydrocarbon solid oxide fuel cells. *Nat. Mater.* **14**, 205–209 (2015).
18. Zhong, M. et al. Accelerated discovery of CO_2 electrocatalysts using active machine learning. *Nature* **581**, 178–183 (2020).
19. Jacobs, R., Mayeshiba, T., Booske, J. & Morgan, D. Material discovery and design principles for stable, high activity perovskite cathodes for solid oxide fuel cells. *Adv. Energy Mater.* **8**, 1702708 (2018).
20. Zhai, S. et al. A combined ionic Lewis acid descriptor and machine-learning approach to prediction of efficient oxygen reduction electrodes for ceramic fuel cells. *Nat. Energy* **7**, 866–875 (2022).
21. Giordano, L. et al. Electronic structure-based descriptors for oxide properties and functions. *Acc. Chem. Res.* **55**, 298–308 (2022).
22. Jacobs, R., Liu, J., Abernathy, H. & Morgan, D. Machine learning design of perovskite catalytic properties. *Adv. Energy Mater.* **14**, 2303684 (2024).
23. Suntivich, J., May, K. J., Gasteiger, H. A., Goodenough, J. B. & Shao-Horn, Y. A perovskite oxide optimized for oxygen evolution catalysis from molecular orbital principles. *Science* **334**, 1383–1385, (2011).
24. Fabbri, E. et al. $Ba_{0.5}Sr_{0.5}Co_{0.8}Fe_{0.2}O_{3-\delta}$ perovskite activity towards the oxygen reduction reaction in alkaline media. *ChemElectroChem* **1**, 338–342 (2014).
25. Pan, Y. et al. Direct evidence of boosted oxygen evolution over perovskite by enhanced lattice oxygen participation. *Nat. Commun.* **11**, 2002 (2020).
26. Li, M., Zhou, W. & Zhu, Z. Comparative studies of $SrCo_{1-x}Ta_xO_{3-\delta}$ (x=0.05–0.4) oxides as cathodes for low-temperature solid-oxide fuel cells. *ChemElectroChem* **2**, 1331–1338 (2015).
27. Herbert, D. E., Lionetti, D., Rittle, J. & Agapie, T. Heterometallic triiron-oxo/hydroxo clusters: effect of redox-inactive metals. *J. Am. Chem. Soc.* **135**, 19075–19078 (2013).
28. Noll, W. The silicate bond from the standpoint of electronic theory. *Angew. Chem., Int. Ed. Engl.* **2**, 73–80 (1963).
29. Wachsman, E. D. & Lee, K. T. Lowering the temperature of solid oxide fuel cells. *Science* **334**, 935–939, (2011).
30. Jablonka, K. M., Ongari, D., Moosavi, S. M. & Smit, B. Using collective knowledge to assign oxidation states of metal cations in metal–organic frameworks. *Nat. Chem.* **13**, 771–777 (2021).
31. Rini, M. et al. Control of the electronic phase of a manganite by mode-selective vibrational excitation. *Nature* **449**, 72–74 (2007).
32. Stern, K. H. & Weise, E. L. *High Temperature Properties and Decomposition of Inorganic Salts.* Part 1. Sulfates. National Bureau of Standards, (1966).
33. Shannon, R. Revised effective ionic radii and systematic studies of interatomic distances in halides and chalcogenides. *Acta Crystallogr., Sect. A* **32**, 751–767 (1976).
34. Pauling, L. The sizes of ions and the structure of ionic crystals. *J. Am. Chem. Soc.* **49**, 765–790 (1927).
35. Matar, S. F., Campet, G. & Subramanian, M. A. Electronic properties of oxides: Chemical and theoretical approaches. *Prog. Solid State Chem.* **39**, 70–95 (2011).
36. Ding, L. et al. Promotion on electrochemical performance of a cation deficient $SrCo_{0.7}Nb_{0.1}Fe_{0.2}O_{3-\delta}$ perovskite cathode for intermediate-temperature solid oxide fuel cells. *J. Power Sources* **354**, 26–33 (2017).
37. Onrubia-Calvo, J. A., Pereda-Ayo, B., Cabrejas, I., De-La-Torre, U. & González-Velasco, J. R. Ba-doped vs. Sr-doped $LaCoO_3$ perovskites as base catalyst in diesel exhaust purification. *Mol. Catal.* **488**, 110913 (2020).
38. Ren, R. et al. Boosting the electrochemical performance of fe-based layered double perovskite cathodes by Zn^{2+} doping for solid oxide fuel cells. *ACS appl. Mater. Inter.* **12**, 23959–23967 (2020).
39. Li, M. R., Zhou, W., Peterson, V. K., Zhao, M. & Zhu, Z. A comparative study of $SrCo_{0.8}Nb_{0.2}O_{3-\delta}$ and $SrCo_{0.8}Ta_{0.2}O_{3-\delta}$ as low-temperature solid oxide fuel cell cathodes: effect of non-geometry factors on the oxygen reduction reaction. *J. Mater. Chem. A* **3**, 24064–24070 (2015).
40. Song, J., Ning, D. & Bouwmeester, H. J. M. Influence of alkaline-earth metal substitution on structure, electrical conductivity and oxygen transport properties of perovskite-type oxides La0.6A0.4 FeO3–δ (A = Ca, Sr and Ba). *Phys. Chem. Chem. Phys.* **22**, 11984–11995 (2020).
41. Zhang, W. et al. Co-incorporating enhancement on oxygen vacancy formation energy and electrochemical property of $Sr_2Co_{1+x}Mo_{1-x}O_{6-\delta}$ cathode for intermediate-temperature solid oxide fuel cell. *Solid State Ion.* **316**, 20–28 (2018).
42. Yang, J. et al. On the ensemble requirement of fully selective chemical looping methane partial oxidation over La-Fe-based perovskites. *Appl. Catal. B: Environ.* **301**, 120788 (2022).
43. Zhao, S. et al. Oxygen vacancy formation and migration in double perovskite Sr_2CrMoO_6: a first-principles study. *RSC Adv.* **6**, 43034–43040 (2016).
44. Olsson, E., Cottom, J., Aparicio-Anglès, X. & de Leeuw, N. H. Computational study of the mixed B-site perovskite $SmB_xCo_{1-x}O_{3-d}$ (B = Mn, Fe, Ni, Cu) for next generation solid oxide fuel cell cathodes. *Phys. Chem. Chem. Phys.* **21**, 9407–9418 (2019).
45. Goodenough, J. B. *Magnetism and the chemical bond*. (Interscience Publishers, 1963).
46. Xu, J. et al. $IrO_x{\cdot}nH_2O$ with lattice water–assisted oxygen exchange for high-performance proton exchange membrane water electrolyzers. *Sci. Adv.* **9**, eadh1718 (2023).
47. Huang, Z.-F. et al. Chemical and structural origin of lattice oxygen oxidation in Co–Zn oxyhydroxide oxygen evolution electrocatalysts. *Nat. Energy* **4**, 329–338 (2019).
48. Roy, C. et al. Impact of nanoparticle size and lattice oxygen on water oxidation on $NiFeO_xH_y$. *Nat. Catal.* **1**, 820–829 (2018).
49. Jacobs, R., Liu, J., Abernathy, H. & Morgan, D. Critical assessment of electronic structure descriptors for predicting perovskite catalytic properties. *ACS Appl. Energy Mater.* **7**, 3366–3377 (2024).
50. Zhu, Y. et al. Promotion of oxygen reduction by exsolved silver nanoparticles on a perovskite scaffold for low-temperature solid oxide fuel cells. *Nano Lett.* **16**, 512–518 (2016).
51. Zhou, W. et al. Novel B-site ordered double perovskite $Ba_2Bi_{0.1}Sc_{0.2}Co_{1.7}O_{6-x}$ for highly efficient oxygen reduction reaction. *Energy Environ. Sci.* **4**, 872–875 (2011).
52. Xu, X. Y. et al. Sc and Ta-doped $SrCoO_{3-\delta}$ perovskite as a high-performance cathode for solid oxide fuel cells. *Compos. B. Eng.* **178**, 107491 (2019).
53. Li, M., Zhou, W. & Zhu, Z. Highly CO_2-tolerant cathode for intermediate-temperature solid oxide fuel cells: samarium-doped ceria-protected $SrCo_{0.85}Ta_{0.15}O_{3-\delta}$ Hybrid. *ACS appl. Mater. Inter.* **9**, 2326–2333 (2017).
54. Zhou, W., Shao, Z., Ran, R. & Cai, R. Novel $SrSc_{0.2}Co_{0.8}O_{3-\delta}$ as a cathode material for low temperature solid-oxide fuel cell. *Electrochem. Commun.* **10**, 1647–1651 (2008).

55. Wang, H. et al. Enhancing catalysis activity of $La_{0.6}Sr_{0.4}Co_{0.8}Fe_{0.2}O_{3-\delta}$ cathode for solid oxide fuel cell by a facile and efficient impregnation process. *Int. J. Hydrog. Energy* **44**, 13757–13767 (2019).
56. Ishfaq, H. A. et al. Boosting performance of the solid oxide fuel cell by facile nano-tailoring of $La_{0.6}Sr_{0.4}CoO_{3-\delta}$ cathode. *Int. J. Hydrog. Energy* **47**, 37587–37598 (2022).
57. Choi, S. et al. Highly efficient and robust cathode materials for low-temperature solid oxide fuel cells: $PrBa_{0.5}Sr_{0.5}Co_{2-x}Fe_xO_{5+\delta}$. *Sci. Rep.* **3**, 2426 (2013).
58. Yoo, S. et al. Development of double-perovskite compounds as cathode materials for low-temperature solid oxide fuel cells. *Angew. Chem. Int. Ed.* **53**, 13064–13067 (2014).
59. Jeong, D. et al. Scandium doping effect on a layered perovskite cathode for low-temperature solid oxide fuel cells (LT-SOFCs). *Appl. Sci.* **8**, 2217 (2018).
60. Zhu, Y., Sunarso, J., Zhou, W., Jiang, S. & Shao, Z. High-performance $SrNb_{0.1}Co_{0.9-x}Fe_xO_{3-\delta}$ perovskite cathodes for low-temperature solid oxide fuel cells. *J. Mater. Chem. A* **2**, 15454–15462 (2014).
61. Li, W. et al. High cationic dispersity boosted oxygen reduction reactivity in multi-element doped perovskites. *Adv. Funct. Mater.* **33**, 2210496 (2023).
62. Simböck, J. et al. Electronic parameters in cobalt-based perovskite-type oxides as descriptors for chemocatalytic reactions. *Nat. Commun.* **11**, 652 (2020).
63. Li, H. B. et al. Electric-field control of ferromagnetism through oxygen ion gating. *Nat. Commun.* **8**, 2156 (2017).
64. Liao, Z., Gao, P., Bai, X., Chen, D. & Zhang, J. Evidence for electric-field-driven migration and diffusion of oxygen vacancies in $Pr_{0.7}Ca_{0.3}MnO_3$. *J. Appl. Phys.* **111**, 114506 (2012).
65. Rehman, A. U. et al. Enhancing oxygen reduction reaction activity and CO_2 tolerance of cathode for low-temperature solid oxide fuel cells by in situ formation of carbonates. *ACS appl. Mater. Inter.* **11**, 26909–26919 (2019).
66. Zhou, W., Liang, F., Shao, Z. & Zhu, Z. Hierarchical CO_2-protective shell for highly efficient oxygen reduction reaction. *Sci. Rep.* **2**, 327 (2012).
67. Gaikwad, P. S., Mondal, K., Shin, Y. K., van Duin, A. C. T. & Pawar, G. Enhancing the Faradaic efficiency of solid oxide electrolysis cells: progress and perspective. *npj Computational Mater.* **9**, 149 (2023).
68. Pinheiro Araújo, T. et al. Flame-made ternary Pd-In_2O_3-ZrO_2 catalyst with enhanced oxygen vacancy generation for CO2 hydrogenation to methanol. *Nat. Commun.* **13**, 5610 (2022).
69. Balaji Gopal, C. et al. Equilibrium oxygen storage capacity of ultrathin $CeO_{2-\delta}$ depends non-monotonically on large biaxial strain. *Nat. Commun.* **8**, 15360 (2017).
70. Snini, K. et al. Synthesis, structural characterization, electric and dielectric properties of $Pr_{0.67}Ba_{0.22}Sr_{0.11}Mn_{0.925}Ni_{0.075}O_3$ perovskite for thermal energy storage. *J. Alloy. Compd.* **874**, 159866 (2021).
71. Gajek, M. et al. Tunnel junctions with multiferroic barriers. *Nat. Mater.* **6**, 296–302 (2007).
72. Chia, X. & Pumera, M. Characteristics and performance of two-dimensional materials for electrocatalysis. *Nat. Catal.* **1**, 909–921 (2018).
73. Mariano, R. G. et al. Microstructural origin of locally enhanced CO_2 electroreduction activity on gold. *Nat. Mater.* **20**, 1000–1006 (2021).
74. Wilson, J. R. et al. Three-dimensional reconstruction of a solid-oxide fuel-cell anode. *Nat. Mater.* **5**, 541–544 (2006).
75. Zhang, Q. et al. Covalent organic framework–based porous ionomers for high-performance fuel cells. *Science* **378**, 181–186 (2022).
76. Wan, C. et al. Amorphous nickel hydroxide shell tailors local chemical environment on platinum surface for alkaline hydrogen evolution reaction. *Nat. Mater.* **22**, 1022–1029 (2023).
77. Geurts, P., Ernst, D. & Wehenkel, L. Extremely randomized trees. *Mach. Learn.* **63**, 3–42 (2006).
78. Breiman, L. Random Forests. *Mach. Learn.* **45**, 5–32 (2001).
79. Freund, Y. & Schapire, R. E. A decision-theoretic generalization of on-line learning and an application to boosting. *J. Comput. Syst. Sci.* **55**, 119–139 (1997).
80. Friedman, J. H. Greedy function approximation: a gradient boosting machine. *Ann. Stat.* **29**, 1189–1232 (2001).
81. Zhang, Y. et al. Thermal-expansion offset for high-performance fuel cell cathodes. *Nature* **591**, 246–251 (2021).
82. Mefford, J. T., Hardin, W. G., Dai, S., Johnston, K. P. & Stevenson, K. J. Anion charge storage through oxygen intercalation in LaMnO3 perovskite pseudocapacitor electrodes. *Nat. Mater.* **13**, 726–732, (2014).
83. Perdew, J. P., Burke, K. & Ernzerhof, M. Generalized gradient approximation made simple. *Phys. Rev. Lett.* **77**, 3865–3868 (1996).
84. Perdew, J. P., Ernzerhof, M. & Burke, K. Rationale for mixing exact exchange with density functional approximations. *J. Chem. Phys.* **105**, 9982–9985 (1996).
85. Kresse, G. & Furthmüller, J. Efficiency of ab-initio total energy calculations for metals and semiconductors using a plane-wave basis set. *Comput. Mater. Sci.* **6**, 15–50 (1996).
86. Perdew, J. P. et al. Restoring the density-gradient expansion for exchange in solids and surfaces. *Phys. Rev. Lett.* **100**, 136406 (2008).
87. Grimme, S. Semiempirical GGA-type density functional constructed with a long-range dispersion correction. *J. Comput. Chem.* **27**, 1787–1799 (2006).
88. Henkelman, G. & Jónsson, H. Improved tangent estimate in the nudged elastic band method for finding minimum energy paths and saddle points. *J. Chem. Phys.* **113**, 9978–9985 (2000).
89. Henkelman, G., Uberuaga, B. P. & Jónsson, H. A climbing image nudged elastic band method for finding saddle points and minimum energy paths. *J. Chem. Phys.* **113**, 9901–9904 (2000).

Acknowledgements

The authors acknowledge the technical assistance from the Center for Microscopy and Microanalysis (CMM) at the University of Queensland and Australian Synchrotron. Z. Zhu and A. Du would like to thank the support from the Australian Research Council (ARC) Discovery Project DP170104660. Z. Zhu also acknowledges the support from ARC DP DP200101397. Z. Li acknowledges the China Scholarship Council (CSC) for awarding a visitor's scholarship (No. 201706450223) in Australia. Y. Luo acknowledges financial support from ARC DE240100105. Y. Luo and Z. Huang acknowledge the support from CE200100025. Z. Huang appreciates the support from ARC DP230101196. We acknowledge support from ARC DE230100637 and the Australian Synchrotron Project (M15364, M15867, and M21058). The authors would like to thank Dr. Jinxuan Zhang's assistance with the scanning electron microscope.

Author contributions

Z.Li. collected literature data for machine learning. M.Li., Y.L., Z.H., Z.S., and Z.Z. conceptualized the project. M.Li., Y.L., X.Xu., Z.Z., D.L., and Z.Y. supervised the project. Y.L., M.Li, and Z.H. conducted feature engineering and machine learning model training and validation. Z.Li and D. F. synthesized the materials, tested the performance and stabilities with the help of X.Xu., M.Li., T.Z., F.L. X.M. and A.Du. performed theoretical investigations. M.Li, L.Z., R.Lin, F.L. performed the material characterizations and analysis. Z.Li. and M.Li. wrote the manuscript.

Competing interests

The authors declare no competing interests.

Additional information

Supplementary information The online version contains supplementary material available at https://doi.org/10.1038/s41467-024-53578-7.

Correspondence and requests for materials should be addressed to Mengran Li, Xiaoyong Xu, Yadan Luo, Zongping Shao or Zhonghua Zhu.

Peer review information *Nature Communications* thanks the anonymous, reviewers for their contribution to the peer review of this work. A peer review file is available.

Reprints and permissions information is available at http://www.nature.com/reprints

Publisher's note Springer Nature remains neutral with regard to jurisdictional claims in published maps and institutional affiliations.

Open Access This article is licensed under a Creative Commons Attribution-NonCommercial-NoDerivatives 4.0 International License, which permits any non-commercial use, sharing, distribution and reproduction in any medium or format, as long as you give appropriate credit to the original author(s) and the source, provide a link to the Creative Commons licence, and indicate if you modified the licensed material. You do not have permission under this licence to share adapted material derived from this article or parts of it. The images or other third party material in this article are included in the article's Creative Commons licence, unless indicated otherwise in a credit line to the material. If material is not included in the article's Creative Commons licence and your intended use is not permitted by statutory regulation or exceeds the permitted use, you will need to obtain permission directly from the copyright holder. To view a copy of this licence, visit http://creativecommons.org/licenses/by-nc-nd/4.0/.

© The Author(s) 2024